RSC Advances

PAPER

View Article Online
View Journal | View Issue

Cite this: *RSC Adv.*, 2025, **15**, 3317

Room temperature sensing of CO_2 using *C*3-symmetry pyridinium-based porous ionic polymers with triazine or benzene cores†

Maha A. Alshubramy,*[a] Khalid A. Alamry, [a] Hajar S. Alorfi,[a] Sameh H. Ismail,[b] Nadjet Rezki, [c] Mohamed Reda Aouad, [c] Salsabeel Al-Sodies[ac] and Mahmoud A. Hussein *[ad]

A new class of ionic polymers tethering triazine (benzene) core hybrids with three dipyridinium as cationic counterparts combined with bromide and/or chloride anions **PPyBz-O$_{Br}$** and **PPyTri-O$_{Cl}$** were successfully prepared *via* the alkylation of 4,4′-dipyridyl derivatives **4,4′-bp-O** with 1,3,5-tris(bromomethyl)benzene **BB** and/or cyanuric chloride **CC**. The precursor, **4,4′-bp-O**,was synthesized through the condensation of 4-pyridine carboxaldehyde and 4,4′-oxydianiline. The resulting ionic polymers, **PPyBz-O$_{Br}$** and **PPyTri-O$_{Cl}$**, underwent metathetical anion exchange, forming new ionic polymers bearing LiTFSI and KPF_6 as anions. Characterization of the synthesized hybrid molecules was performed through FTIR, ^1H NMR, and ^{13}C NMR analyses. PXRD and SEM showed semi-crystalline structures and a homogenous distribution of micro-/or nanoparticles. TGA and DTA displayed high thermal stability of the synthesized polymer. The sensing activity of the modified ionic polymers was examined using a quartz crystal nanobalance (QCN) for CO_2 detection. The resulting sensor demonstrated the ability to provide precise, selective, and reproducible CO_2 measurements.

Received 1st October 2024
Accepted 16th January 2025

DOI: 10.1039/d4ra07062c

rsc.li/rsc-advances

1. Introduction

The detection of carbon dioxide (CO_2) is pivotal across diverse domains, including fire detection,[1] greenhouse gas surveillance,[2] air-quality monitoring,[3,4] health,[5–7] marine and environmental studies,[8] and food supply chain management.[9,10] Traditional CO_2 sensing methods, such as gas chromatography,[11] infrared spectrometry,[12] fluorescence,[13–15] photoacoustic spectroscopy,[16] and severinghaus electrodes,[17] offer high selectivity and sensitivity. However, they often suffer from drawbacks such as high costs, bulkiness, elevated power consumption, and susceptibility to electromagnetic interference.[16,18] The development of highly sensitive, efficient, and cost-effective sensors is critical for on-site analysis and reducing CO_2 emissions. The quartz crystal nanobalance (QCN) is a device that utilizes a quartz crystal microbalance (QCM) to detect mass changes at the nanogram level by measuring changes in the resonator frequency. By incorporating an appropriate chemical interface layer or recognition element, the QCN exhibits significant potential for CO_2 sensing.[19]

CO_2-responsive polymers have garnered significant attention due to their high flexibility and sensitivity at room temperature.[20–24] These polymers undergo changes in physical attributes, such as electrical resistance, volume, and transparency, when exposed to CO_2.[25] Among the functional groups in these polymers, amidine,[26,27] guanidine,[28] and amines,[29,30] especially tertiary amines, have been extensively studied for their CO_2 responsiveness. Tertiary amines, with moderate base properties, exhibit good switchability between neutral and charged states. In contrast, primary and secondary amines form carbamate salts in the presence of CO_2, making them less suitable for sensing applications.[31–33]

In recent years, considerable efforts have been made dedicated to the design, synthesis, and development of focused macromolecules with significant electrochemical features, which are the aims associated with various applications in organic synthesis. A wide range of porous materials such as covalent organic frameworks (COFs),[34] porous organic polymers (POPs),[35] metal–organic frameworks (MOFs),[36] organic–inorganic hybrid materials[37] *etc.*, are attractive scaffolds for designing and developing various applications such as gas storage,[38–41] photovoltaics,[42] conductivity,[43–45] batteries,[46–50] catalysis,[51–54] optoelectronic devices,[55] and electrochemical sensing.[56]

---

[a] *Chemistry Department, Faculty of Science, King Abdulaziz University, Jeddah 21589, Saudi Arabia. E-mail: maha.alshubramy@gmail.com; malshubramy@stu.kau.edu.sa; maabdo@kau.edu.sa*

[b] *Egypt Nanotechnology Center, Cairo University, El–Sheikh Zayed, 6th October, Giza, Egypt*

[c] *Department of Chemistry, Taibah University, 30002, Al-Madina Al-Mounawara, Saudi Arabia*

[d] *Chemistry Department, Faculty of Science, Assiut University, Assiut, 71516, Egypt. E-mail: mahussein74@yahoo.com*

† Electronic supplementary information (ESI) available. See DOI: https://doi.org/10.1039/d4ra07062c

While various advanced porous materials such as zeolites,[57] metal–organic frameworks (MOFs),[58] ionic liquids,[59,60] phenolic resins, activated carbons, and carbon composites[61] have been explored, POPs, particularly those with porous frameworks containing C–N linkages, have emerged as promising candidates for CO_2 sensing. The dipole–dipole interaction between CO_2 and N atoms in these frameworks enhances their effectiveness.[62–64] One of the effective methods for incorporating C–N functional groups is to synthesize triazine with the rigid-shaped structure and *C*3-symmetry, utilizing a simple synthetic method not only without the formation of byproducts but also without the need for any kind of catalyst. Moreover, the other N-rich functionalities, such as pyridine, amine, amide, carbazole, or porphyrin units, need to be designed and synthesized reasonably, which have been proven to be efficient functional materials for gas storage/separation, heterogeneous catalysis, and sensing.[65,66]

However, the performance of QCM sensors depends significantly on the properties of the coating material used. Previous studies have explored a range of materials, including acrylonitrile–styrene copolymers (AS), tetramethylammonium fluoride tetrahydrate (TMAF), and polyethyleneimine (PEI) coatings. For example, AS-coated QCM sensors showed sensitivity to CO_2 but were also highly affected by humidity, limiting their specificity for CO_2 in mixed-gas environments.[67] Similarly, TMAF-coated QCM sensors demonstrated sensitivity to multiple gases such as SO_2, NH_3, and CO_2, with limited selectivity for CO_2.[68] More recently, multilayered systems involving materials such as PEI and nitrogen-doped tungsten carbide (WC@NC) have shown promise in mixed-gas classification but are complex to fabricate and optimize.[69] Despite these advances, challenges remain in achieving high sensitivity, selectivity, and thermal stability for CO_2 detection using QCM-based sensors. In this context, the design of porous materials with tailored functionalities presents a promising approach. Porous ionic polymers (PIPs), particularly those combining nitrogen-rich frameworks and electrostatic interaction sites, offer significant potential for CO_2 sensing. However, previous work in this area has been limited by the lack of synergistic design elements that enhance both adsorption and sensor performance. In this study, we report a new class of porous ionic polymers (PIPs) designed for CO_2 sensing, incorporating triazine (benzene) cores and pyridinium cations with PF_6 and TFSI anions. The unique combination of triazine and pyridinium units introduces several advantages. The triazine core provides a nitrogen-rich, semi-crystalline framework with high thermal stability, enabling robust performance in harsh conditions. Pyridinium cations introduce electrostatic interaction sites, increasing affinity for CO_2 molecules while maintaining selectivity over NH_3 and H_2S. Furthermore, the incorporation of PF_6 and TFSI anions influences the material's morphology and crystallinity, optimizing gas diffusion and adsorption.

2. Experimental

2.1. Synthesis of *N*,*N*′-(oxybis(4,1-phenylene))bis(1-(pyridin-4-yl)methanimine) 4,4′-bp-O

A mixture of 4-pyridine carboxaldehyde (2 mmol) and 4,4′-oxydianiline (1 mmol) was dissolved in ethanol (25 mL) with drops of conc. HCl as a catalyst. The reaction mixture was heated under reflux for 3 h. Then, the precipitate formed was filtered, washed thoroughly with ethanol, dried, and recrystallized from acetone to give the desired Schiff bases **4,4′-bp-O**. It was obtained as white crystals in 90%, Mp = 250 °C. FTIR (ν, cm^{-1}): 3016 (s, Ar–H stretch), 1622 (C=N, imine), 1596 (C=N, pyridine), 1460 (Ar C=C bending), 1082 (Ar C–N bending), 829 (Ar C=C bending). ^1H NMR (400 MHz, DMSO-d_6): $\delta_H = 7.14$ (d, 4H, $J = 5.48$ Hz, Ar–H), 7.45 (d, 4H, $J = 5.84$ Hz, Ar–H), 7.86 (d, 4H, $J = 3.96$ Hz, Ar–H), 8.75 (s, 2H, HC=N), 8.76 (d, 4H, $J = 3.96$ Hz, Ar–H). ^{13}C NMR (DMSO-d_6, 200 MHz): $\delta_C = 158$, 156, 150, 146, 143, 123, 122, 119.

2.2. Synthesis of dipyridinium cationic polymers-based triazine and/or benzene core PPyBz-O_{Br} and PPyTri-O_{Cl}

To a solution of 4,4′-dipyridyl, **4,4′-bp-O** (1.5 mmol) in acetonitrile (20 mL) was added dropwise a solution 1,3,5-tris(-bromomethyl)benzene **BB** and/or cyanuric chloride **CC** in acetonitrile (20 mL) under stirring. The reaction mixture was then refluxed for 72 h. The precipitate formed was collected by filtration, washed with chloroform (3 × 15 mL) dried to the desired ionic polymers **PPyBz-O_{Br}** and **PPyTri-O_{Cl}**.

2.2.1 Characterization of polymer PPyBz-O_{Br}. **PPyBz-O_{Br}** was obtained as a yellow powder in 95% yield, FTIR: ν [cm^{-1}]: 3385 (pyridinium salt stretch), 3116 (alkenyl C–H stretch), 3016 (Ar C–H stretch), 2970 (Alkyl C–H stretch), 1636 (pyridinium salt ring vibration), 1460 (Ar C=C bending), 1160 (Ar C–N bending), 829 (Ar C–C bending). ^1H NMR (850 MHz, DMSO): δ (ppm) 8.77 (s, 1H), 8.49 (m, 2H), 8.29 (m, 2H), 8.02 (s, 1H), 7.94–7.33 (m, 4H), 5.80 (m, 2H). ^{13}C NMR (400 MHz, DMSO): δ(ppm) 160.21, 149.96, 147.92, 145.22, 144.47, 140.07, 134.23, 132.76, 130.71, 129.54, 126.76, 66.06.

2.2.2 Characterization of polymer PPyTri-O_{Cl}. **PPyTri-O_{Cl}** was obtained as a brown powder in 75% yield, FTIR: ν [cm^{-1}]: 3423 (pyridinium salt stretch), 3116 (alkenyl C–H stretch), 3016 (Ar C–H stretch), 1636 (pyridinium salt ring vibration), 1593 (triazine C=N), 1384 (C–N bending) 1460 (Ar C=C bending), 1160 (Ar C–N bending), 829 (Ar C–C bending). ^1H NMR (850 MHz, DMSO): δ (ppm) 8.81 (m, 2H), 8.59 (m, 2H), 8.34 (m, 1H), 8.25–8.01 (m, 2H), 7.62–7.28 (m, 2H). ^{13}C NMR (400 MHz, DMSO): δ (ppm) 171.86, 166.97, 155.94, 152.24, 141.35, 138.27, 133.66, 122.06.

2.3. Metathesis synthesis of ionic polymers PPyBz-O_{PF6}, PPyBz-O_{TFSI}, PPyTri-O_{PF6} and PPyTri-O_{TFSI}

To a solution of ionic polymers **PPyBz-O_{Br}** and **PPyTri-O_{Cl}** (1 mmol) in acetonitrile was added a solution of lithium bis(trifluoromethane)sulfonimide (LiTFSI) and/or potassium hexafluorophosphate (KPF_6) (1.2 mmol) and the solution was refluxed for 24 h. The solid formed was collected by filtration, washed with deionized water and dried at 100 °C.

2.3.1 Characterization of polymer PPyBz-O_{PF6}. **PPyBz-O_{PF6}** was obtained as a yellowish-orange powder in 90% yield, FTIR: ν [cm^{-1}]: 3423 (pyridinium salt stretch), 3116 (alkenyl C–H stretch), 3016 (Ar C–H stretch), 2970 (Alkyl C–H stretch), 1636 (pyridinium salt ring vibration), 1460 (s, Ar C=C bending), 1160 (Ar C–N bending), 829 (Ar C–C bending), 863 ($PF6^-$). ^1H NMR (850 MHz, DMSO): δ (ppm) 8.85 (s, 1H), 8.59 (m, 2H), 8.41 (m, 2H), 8.15 (s, 1H), 8.03–7.37 (m, 4H), 5.92 (m, 2H). ^{13}C NMR (400 MHz, DMSO): δ(ppm) 160.21, 148.24, 147.71, 145.16, 144.92, 140.31, 134.28, 132.98, 130.84, 129.83, 128.49, 126.87, 67.06. ^{31}P NMR (162 MHz, DMSO) δ −131.01 to −157.36 (sep). ^{19}F NMR (377 MHz, DMSO) δ −69.18 (s), −71.07 (s).

2.3.2 Characterization of polymer PPyBz-O$_{TFSI}$. **PPyBz-O$_{TFSI}$** was obtained as a light orange powder in 90%, FTIR: ν [cm^{-1}]: 3423 (pyridinium salt stretch), 3116 (alkenyl C–H stretch), 3016 (Ar C–H stretch), 2970 (alkyl C–H stretch), 1636 (pyridinium salt ring vibration), 1460 (Ar C=C bending), 1160 (Ar C–N bending), 829 (Ar C–C bending), 1207 (SO_2, TFSI) and 1353 (CF_3, TFSI). ^{1}H NMR (850 MHz, DMSO): δ (ppm) 8.85 (s, 1H), 8.59 (m, 2H), 8.41 (m, 2H), 8.15 (s, 1H), 8.03–7.37 (m, 4H), 5.92 (m, 2H). ^{13}C NMR (400 MHz, DMSO): δ(ppm) 160.05, 148.16, 147.81, 145.36, 144.64, 140.23, 134.16, 132.74, 130.03, 128.65, 126.76, 66.98. ^{19}F NMR (377 MHz, DMSO): δ(ppm) −73.49 (s).

2.3.3 Characterization of PPyTri-O$_{PF6}$. **PPyTri-O$_{PF6}$** was obtained as a reddish-brown powder in 90% yield, FTIR: ν [cm^{-1}]: 3423 (pyridinium salt stretch), 3116 (alkenyl C–H stretch), 3016 (Ar C–H stretch), 1636 (pyridinium salt ring vibration), 1593 (triazine C=N), 1384 (C–N^{+} bending)1460 (Ar C=C bending), 1160 (Ar C–N bending), 829 (Ar C–C bending), 863 ($PF6^{-}$). ^{1}H NMR (850 MHz, DMSO): δ (ppm) 8.87 (m, 2H), 8.67 (m, 2H), 8.39 (s, 1H), 8.33–8.19 (m, 2H), 7.73–7.38 (m, 2H). ^{13}C NMR (400 MHz, DMSO): δ (ppm) 171.79, 167.11 154.94, 152.24, 141.18, 138.41, 133.76, 121.99. ^{31}P NMR (162 MHz, DMSO) δ −131.01 to −157.36 (sep). ^{19}F NMR (377 MHz, DMSO) δ −69.17 (s), −71.06 (s).

2.3.4 Characterization of polymer PPyTri-O$_{TFSI}$. **PPyTri-O$_{TFSI}$** obtained as a brown powder in 95% yield, FTIR: ν [cm^{-1}]: 3423 (s, pyridinium salt stretch), 3116 (w, alkenyl C–H stretch), 3016 (s, Ar C–H stretch), 1636 (*vs.*, pyridinium salt ring vibration), 1593 (s, triazine C=N), 1384 (s, C–N^{+} bending)1460 (s, Ar C=C bending), 1160 (s, Ar C–N bending), 829 (*vs.*, Ar C–C bending), 1207 (SO_2, TFSI) and 1353 (CF_3, TFSI). ^{1}H NMR (850 MHz, DMSO): δ (ppm) 8.77 (m, 2H), 8.55 (m, 2H), 8.30 (s, 1H), 8.21–8.06 (m, 2H), 7.60–7.25 (m, 2H). ^{13}C NMR (400 MHz, DMSO): δ (ppm) 171.93, 167.04 155.94, 152.31, 141.03, 138.41, 133.76, 122.06. ^{19}F NMR (377 MHz, DMSO) δ −73.49 (s).

2.4. Fabrication of PPyTri-O and PPyBz-O CO_2 sensors

The QCN was used to evaluate the **PPyTri-O** and **PPyBz-O** activity toward CO_2 detection. In order to ensure a clean surface, the piranha solution (a blend of sulfuric acid and hydrogen peroxide) was used to clean the QCN chips, and the samples

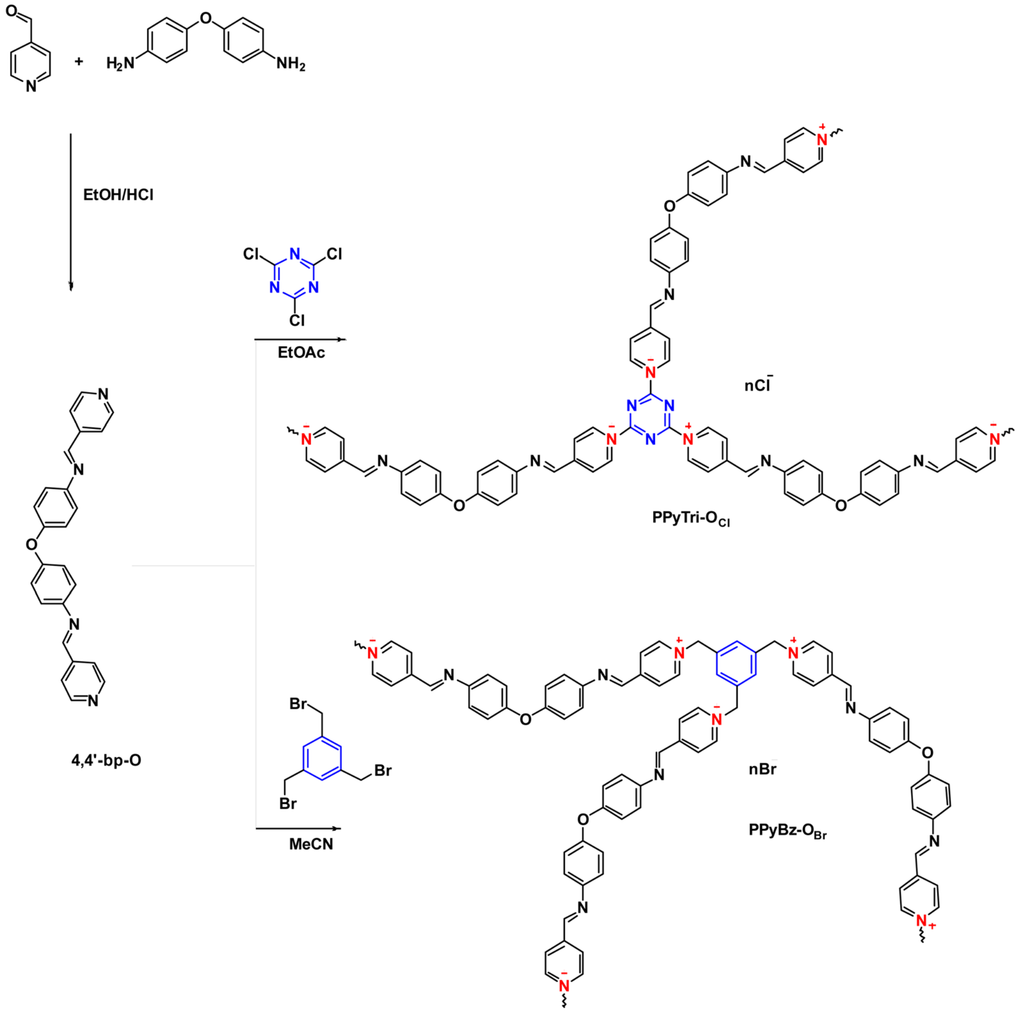

Scheme 1 Synthesis of the precursor Schiff base **4,4′-bp-O** and targeted *C*3-symmetry porous ionic polymers **PPyBz-O$_{Br}$**, **PPyTri-O$_{Cl}$**.

were rinsed with deionized water and dried using nitrogen. To create conductive pathways for the PIP sensors, the gold electrode was deposited on the QCN chip using a sputtering deposition method. The PIP layers were then applied using the spin coating technique and connected to the measurement system using bond wires. The CO_2 chamber was prepared by installing inlets and outlets for gas flow and a temperature control system of 20 °C, 25 °C, and 30 °C using Peltier temperature baths. CO_2 gas was then introduced into the chamber, and the sensor responses were analyzed to evaluate the performance of the PIP sensors under different temperature conditions.

3. Results and discussion

3.1. Synthesis and characterization

The design of *C*3-symmetry porous ionic polymers (PIPs) involved careful consideration of the core structure and linkers. Thus, in the present work, new ionic polymers with a *C*3-symmetry structure were synthesized and investigated for their CO_2 detection. The benzene and/or triazine core, viologen as linkers, and PF_6^- and $TFSI^-$ as counter anions were combined in the same framework of the tailored polymers in order to improve the electrostatic and aromatic properties impacting their overall behavior as well as CO_2 sensing. The synthesis of the targeted *C*3-symmetry pyridinium ionic polymers **PPyBz-O$_{Br}$**, **PPyBz-O$_{PF6}$**, **PPyBz-O$_{TFSI}$**, **PPyTri-O$_{Cl}$**, **PPyTri-O$_{PF6}$**, and **PPyTri-O$_{TFSI}$** was accomplished using the synthetic methodology depicted in Schemes 1 and 2. The first step involved the synthesis of the precursor's Schiff base **4,4′-bp-O** through thermal condensation of the 4-pyridine carboxaldehyde with 4,4′-oxydianiline in refluxing ethanol and in the presence of the catalytic amount of acid. The ^1H NMR spectra of the monomer **4,4′-bp-O** showed characteristic signals at 7.14–8.76 ppm and 7.09–8.76 ppm attributed to the aromatic protons of the phenyl

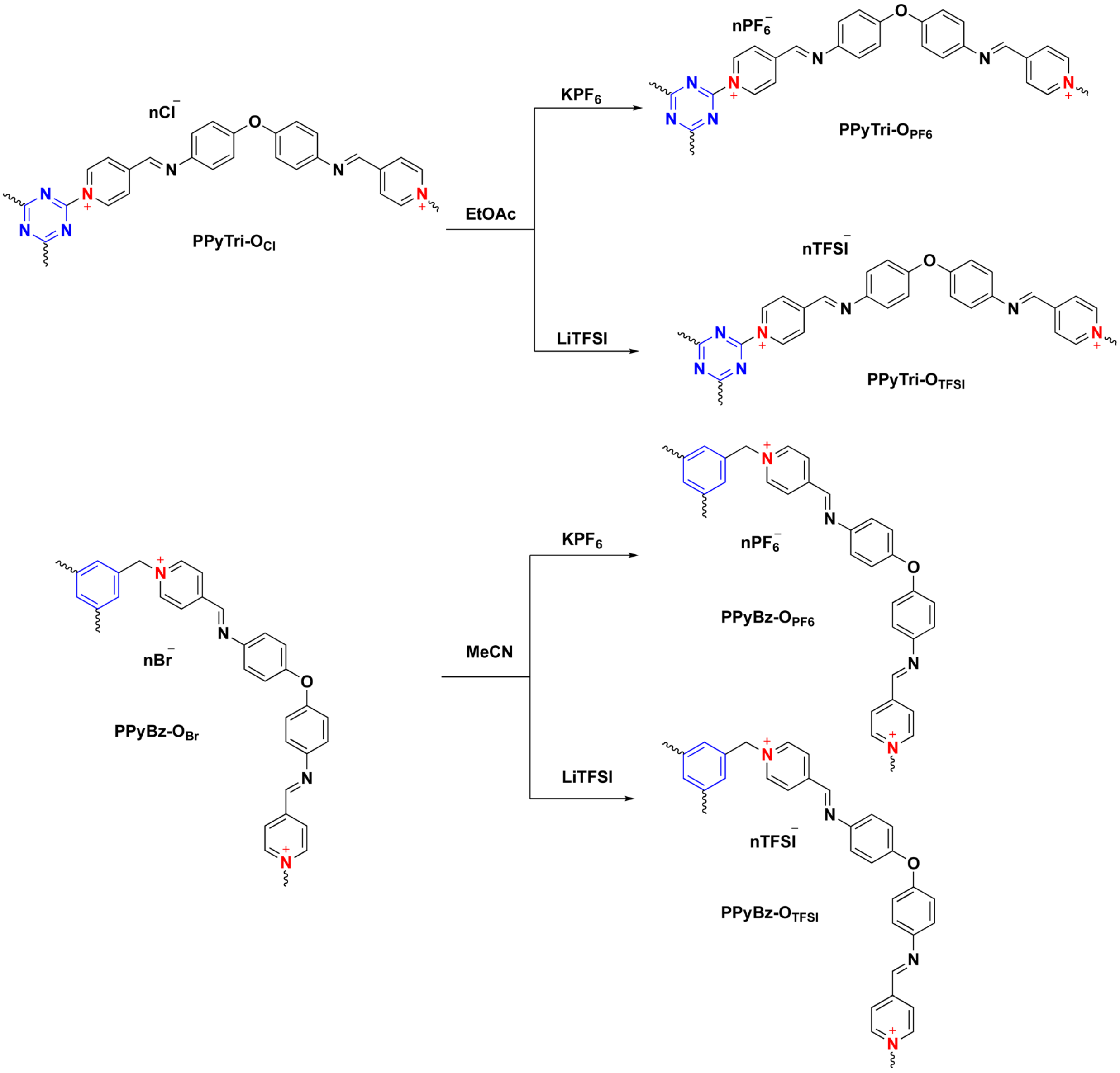

Scheme 2 Metathesis of *C*3-symmetry porous ionic polymers.

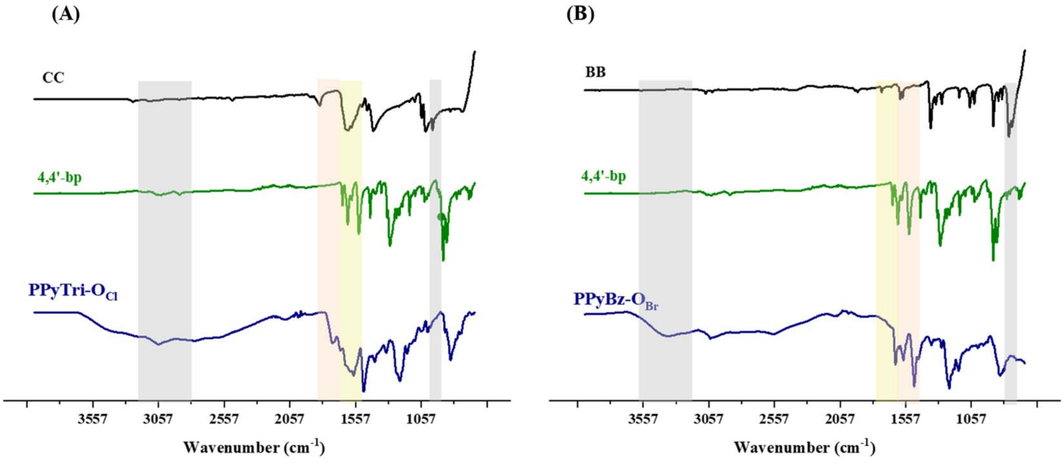

Fig. 1 FTIR spectra of the precursor Schiff base **4,4′-bp-O** and targeted *C*3-symmetry porous ionic polymers. (A) Triazine core and (B) benzene core.

and pyridine rings, respectively. While the imine proton (HC=N) appeared as a distinct singlet at 8.75 ppm.

The Menshutkin reaction was adopted as a common method for generating polymers-based quaternary pyridinium as ammonium salt. Thus, the appropriate 1,3,5-tris(bromomethyl) benzene **BB** and/or cyanuric chloride **CC** were used in the polymerization process through their conjunction with the synthesized bis(1-(pyridin-4-yl)methanimine) Schiff base **4,4′-bp-O** as linkers to furnish the desired cationic polymers **PPyBz-O$_{Br}$** and **PPyTri-O$_{Cl}$** bearing chloride and bromide as counter anions, as elucidated in Scheme 1. The success of the synthesis of the targeted *C*3-symmetry ionic polymers was supported by the investigation of their spectral data based on FTIR and NMR results. Thus, the FTIR spectrum of the polymer **PPyTri-O$_{Cl}$** (Fig. 1(A)) clearly showed the disappearance of the stretching vibration near 850 cm^{-1} attributed to the C–Cl band of the starting material **CC**, supporting the quaternization of pyridine ring in the monomer **4,4′-bp-O**. A new intense band was observed near 1645 cm^{-1} belonging to pyridinium cations, which is another piece of evidence for the success of the quaternization reaction and formation of the targeted ionic polymers **PPyTri-O$_{Cl}$**. The spectra also showed a shift of the C=N absorption bands of the triazine ring (1508 cm^{-1}) compared to their precursor **CC**. The C=N absorption of the azomethine linkage and pyridine ring were observed at 1630 and 1650 cm^{-1}, respectively. Similarly, no stretching bands near 690 cm^{-1} were recorded in the FTIR spectra of the polymers tethering to the benzene core **PPyBz-O$_{Br}$** (Fig. 1(B)), confirming the absence of the C–Br bond in their structure and confirming their involvement in the alkylation of the pyridine nucleus yielding the desired adduct **PPyBz-O$_{Br}$**, with the quaternary nitrogen atoms (N$^+$) exhibiting an intense band around 1645 cm^{-1}, evidencing the proposed structures. In addition, the band observed at 1640 cm^{-1} confirmed the presence of the imine linkage in the framework of the resulting **PPyBz-O$_{Br}$** ionic polymer.

On the other hand, the structures of the synthesized polymers **PPyBz-O$_{Br}$**, **PPyBz-O$_{PF6}$**, **PPyBz-O$_{TFSI}$**, **PPyTri-O$_{Cl}$**, **PPyTri-O$_{PF6}$**, and **PPyTri-O$_{TFSI}$** were elucidated based on their NMR spectra. The ^{1}H NMR spectra of the developed polymers-based triazine core **PPyTri-O$_{Cl}$** and their analogs **PPyTri-O$_{PF6}$** and **PPyTri-O$_{TFSI}$** (Fig. 2(A)) exhibited a broad signal in the aromatic

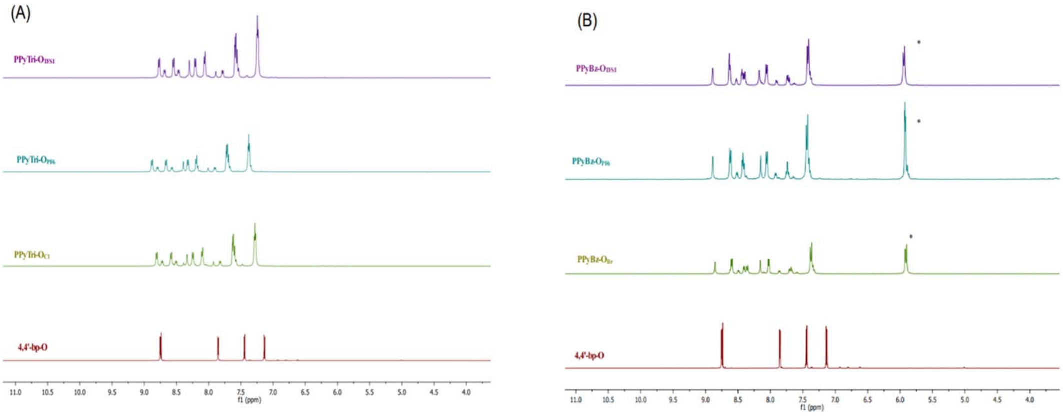

Fig. 2 ^{1}H NMR spectra of the precursor Schiff base **4,4′-bp-O** and the targeted *C*3-symmetry porous ionic polymers. (A) Triazine core and (B) benzene core.

area ranging from 7.25 to 8.87 ppm due to the polymeric backbone effect. The imine protons resonated around 8.30–8.39 ppm. Moreover, the carbons of the triazine ring and imine were recorded at 171.86–171.93 ppm and 166.97–167.04 ppm, respectively, in their ^{13}C NMR spectra. The remaining aromatic carbons were observed in their appropriate area (121.80 to 155.94 ppm) and are detailed in the experimental section.

The ^{1}H NMR of the polymers comprising the benzene nucleus, **PPyBz-O$_{Br}$**, **PPyBz-O$_{PF6}$**, and **PPyBz-O$_{TFSI}$** (Fig. 2(B)), revealed additional signals at 5.80 to 5.94 ppm attributed to methylene protons (CH$_2$), confirming the incorporation of the benzene core in the polymer structures resulting from the quaternization reaction. Their NMR spectra revealed the same broadness as appeared on the first set of the triazine-ionic polymers. The spectra also displayed characteristic singlets at 8.02, 8.19, and 8.15 ppm belonging to the imine protons (CH=N) with the same shift impact that seemed in the triazine core results. Extra aromatic protons resonated at 8.77 and 8.85 ppm confirming the presence of the benzene rings. The ^{13}C NMR spectra showed new signals ranging from 66.06 to 66.98 ppm, revealing the presence of the methylene carbons (CH$_2$).

The resulting cationic polymers, **PPyBz-O$_{Br}$** and **PPyTri-O$_{Cl}$**, which incorporate chloride (Cl$^-$) and bromide (Br$^-$) as counter anions, undergo a metathesis reaction. This anion exchange process occurs when the polymers are treated with a saturated brine solution of LiTFSI and KPF$_6$, yielding the cationic polymers with PF$_6$$^-$ and TFSI$^-$ as counter anions: **PPyBz-O$_{PF6}$**, **PPyBz-O$_{TFSI}$**, **PPyTri-O$_{PF6}$** and **PPyTri-O$_{TFSI}$**. The success of the metathesis reaction was confirmed and supported by the investigation of the spectral data of the resulting polymers **PPyBz-O$_{PF6}$**, **PPyBz-O$_{TFSI}$**, **PPyTri-O$_{PF6}$** and **PPyTri-O$_{TFSI}$** tethering the PF$_6$ and TFSI as counter anions. Their FTIR spectra (Fig. S1†) showed the appearance of the absorption bands at 863 cm^{-1}, 1207 cm^{-1}, and 1353 cm^{-1}, confirming the presence of PF6$^-$, SO$_2$, and CF$_3$, respectively, of TFSI$^-$ anions. The analysis of ^{19}F NMR and ^{31}P NMR (Fig. S2†) of the polymers **PPyBz-O$_{PF6}$**, **PPyBz-O$_{TFSI}$**, **PPyTri-O$_{PF6}$**, and **PPyTri-O$_{TFSI}$** were in accordance with their structures. The polymers **PPyBz-O$_{PF6}$** and **PPyTri-O$_{PF6}$** displayed distinguished two singlets at −69.17 and −71.06 ppm and −69.18 and −71.07 ppm, respectively. In addition, the PF$_6$$^-$ anion exchange was also confirmed from the resonance of distinct septet in the range of −131.01 to −157.36 ppm appearing in the ^{31}P NMR spectra of **PPyBz-O$_{PF6}$** and **PPyTri-O$_{PF6}$** polymers. The TFSI$^-$ anions appeared as a singlet near −73.49 ppm in the ^{19}F NMR spectra of **PPyBz-O$_{TFSI}$** and **PPyTri-O$_{TFSI}$** polymers supporting their structures (Fig. S2†).

3.2. Morphology study

Powder X-ray diffraction (PXRD) was utilized to analyze the crystalline nature of the synthesized polymers (Fig. 3). The PXRD patterns showed semi-crystalline behavior for all formed polymers, with four main characteristic peaks at $2\theta = 19.3°$, 26.4°, 54.4°, and 72.9°. The diffraction peaks at $2\theta = 10°–30°$ and $2\theta = 35°–50°$ were the confirmation of the (002) and (101) planes of the carbon materials, respectively. The peak at 10°–30° indicated the fragmented and devolved crystallite aromatic structure, while a broad and weak peak at 35°–50° indicated an amorphous structure with minimal graphitization degree.[70]

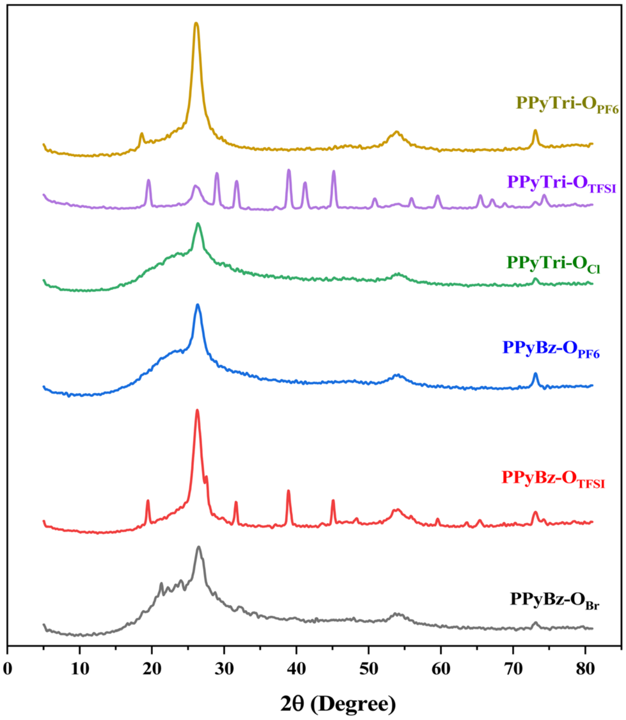

Fig. 3 PXRD patterns of the synthesized *C*3-symmetry porous ionic polymers.

The exchange anions affected the crystallinity of the designed two core polymers due to the flexible structure *via* the imine and aliphatic bridges between the rigid aromatic rings. The anions displacement by the TFSI anion in **PPyBz-O$_{TFSI}$** and **PPyTri-O$_{TFSI}$** polymers caused an increase in the crystallinity in the PXRD patterns and showed diffraction peaks at 19.5°, 28.9°, 31.7°, 39.0°, 45.1° that matched (201), (114), (015), (116), (125) crystal planes, respectively, and were consistent with the data from the JCPDS card (no: 01-082-2341) of TFSI. The bulky size of the TFSI ion affected the natural crystal packing due to the formation of the bilayer structure with no significant change in the crystallinity of PF$_6$. This structural flexibility has also been reported in porous materials.[71–73]

To obtain in-depth insight into the impact of the anions on the morphology of the *C*3-symmetry porous ionic polymers, the synthesized polymers were examined using scanning electron microscopy (SEM) at a magnification of 20 k*x*, as shown in (Fig. 4(A–F)). In the case of the polymers **PPyTri-O** and **PPyBz-O**, distinct and well-defined morphologies were observed, featuring sphere-shaped structures with sizes ranging from nanosized. Conversely, both **PPyTri-O$_{PF6}$** and **PPyBz-O$_{PF6}$** exhibited aggregated clusters, coarse surfaces, and loosely arranged irregular particles. Similarly, the polymers **PPyTri-O$_{TFSI}$** and **PPyBz-O$_{TFSI}$** showed aggregated and irregular particles in the micron-scale dimensions. These SEM images vividly depict the significant impact of bulky anions on the polymer morphology. This observation aligns with findings reported by E. Maya *et al.*[74]

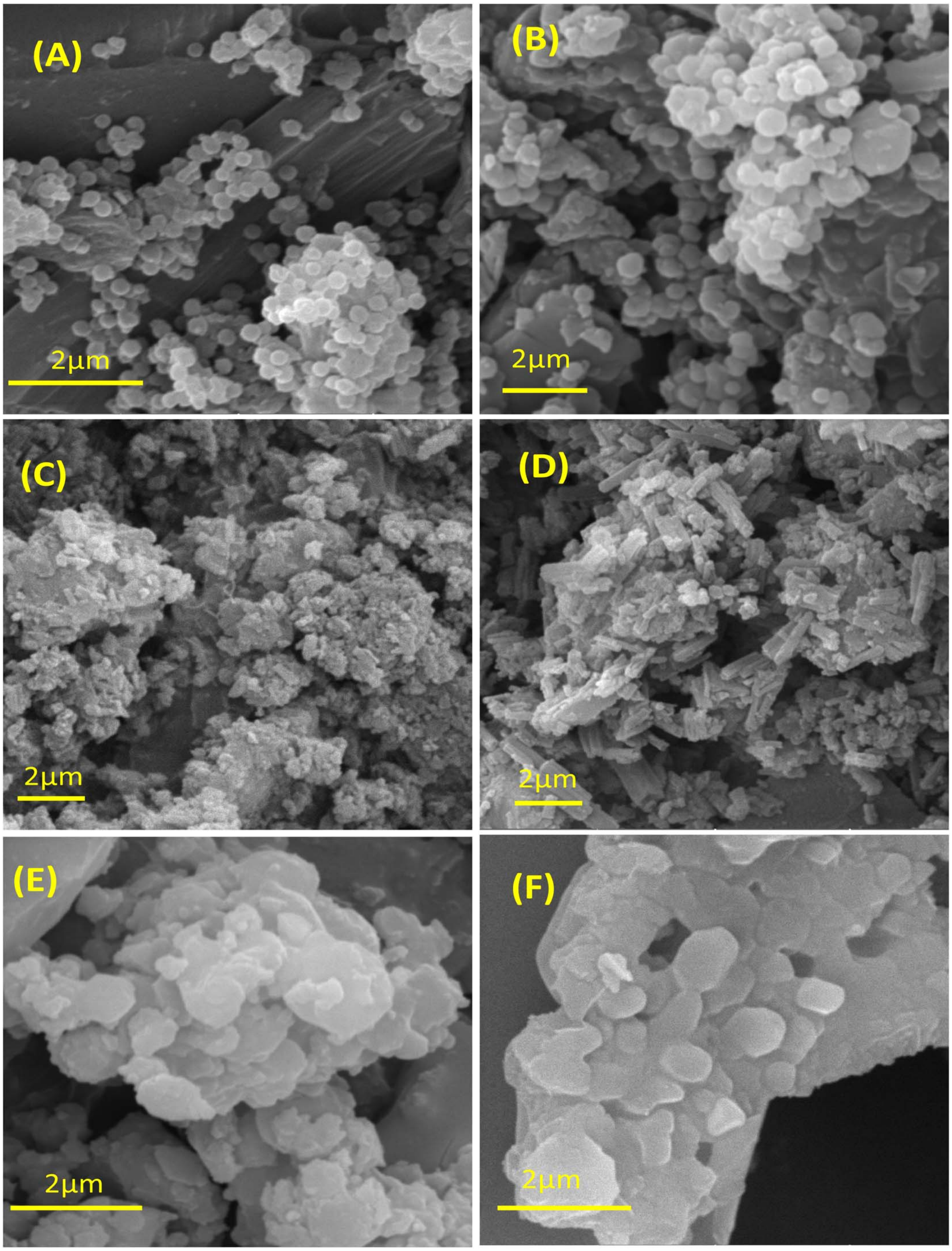

Fig. 4 SEM images of the synthesized porous ionic polymers with *C*3-symmetry (A) **PPyBz-O$_{Br}$**, (B) **PPyTri-O$_{Cl}$**, (C) **PPyBz-O$_{PF6}$**, (D) **PPyTri-O$_{PF6}$**, (E) **PPyBz-O$_{TFSI}$** and (F) **PPyTri-O$_{TFSI}$**.

3.3. Thermal study

The thermal properties of the synthesized *C*3-symmetry ionic polymers were studied using thermogravimetric analysis (TGA) and derivative thermogravimetry (DTG) in the temperature range of 25–1000 °C at a heating rate of 10 °C min^{-1} (Fig. S3†). The TGA/DTG curves exhibited three-step weight loss. Most synthesized polymers were not hygroscopic in nature, and the first stage of weight loss occurred between 200 °C and 600 °C, while the second stage was observed between 630 °C and 840 °C owing to the degradation of the polymer backbone.[70,75–77]

Table 1 presents a comprehensive comparison of T_{10}, T_{25}, and T_{50}, illustrating thermal decomposition at 10%, 25%, and 50%, respectively, for the polymers. The values of T_{10}, T_{25}, and T_{50} in the case of triazine core, the polymer with PF6 anion has the highest thermal stability, while in the case of benzene core, the anion with TFSI has the highest thermal stability. Moreover, Table 1 outlines the final temperature for the polymer

Table 1 Thermal behavior of the synthesized *C*3-symmetry porous ionic polymers

	$T_{10\%}$	$T_{25\%}$	$T_{50\%}$	T_{final}	$T_{\max}$
PPyTri-O$_{\mathrm{Cl}}$	280	320	380	740	690
PPyTri-O$_{\mathrm{PF6}}$	270	370	470	680	700
PPyTri-O$_{\mathrm{TFSI}}$	220	360	400	830	800
PPyBz-O$_{\mathrm{Br}}$	230	275	360	765	730
PPyBz-O$_{\mathrm{PF6}}$	160	190	300	685	670
PPyBz-O$_{\mathrm{TFSI}}$	300	370	460	770	720

degradation (PDT$_{\text{final}}$) and the maximum polymer decomposition temperature (PDT$_{\max}$). As exemplified by Table 1, the PDT$_{\text{final}}$ values ranged from 680 °C to 830 °C, while the DTG revealed PDT$_{\max}$ in the range of 670–800 °C. The bulky anion TFSI with triazine core shows the highest lowest values of PDT$_{\text{final}}$ and PDT$_{\max}$ in comparison with the other anions. While the polymers with PF6 anion have the same value of PDT$_{\text{final}}$ in two cores; however, the PDTmax value shows the highest thermal stability in the triazine core. From the polymers under investigation, it was found that the triazine core had more thermal stability, which may be due to less flexibility, and the bulky anion TFSI also increases the thermal stability by increasing the electrostatic effect.

3.4. Nitrogen adsorption analysis

Nitrogen adsorption–desorption isotherms, as shown in Fig. S4,† were taken to characterize the pores in the *C*3-symmetry ionic polymer. All the polymers exhibited type IV nitrogen adsorption–desorption isotherms.[78] The adsorption equilibrium leads to the growth of the H3 hysteresis loop, associated with capillary condensation in mesoporous structures, including the accumulation of the slit pore formation.[79] Table 2 shows the specific surface area calculated using the Bruner–Emmett–Teller (BET) theory model and density functional theory (DFT), as well as pore volume and average pore size calculated using the BJH model and DFT. Accordingly, the pore-size distributions were evaluated through BJH and DFT, approved mesopores character (more than 2 nm pores) for all the pore-size distribution patterns (Fig. S4†). Table 2 shows that the polymers with the triazine core have a higher specific surface area when compared with polymers with benzene cores for the same anion. That may be due to the flexibility of methylene in the benzene core that reduces the surface area.[80] However, when the anion is exchanged by PF$_6$ or TFSI for the same core, it is found that TFSI has a lower surface area compared to PF$_6$. The same pattern is found in the benzene and triazine cores, and that may affect the bulky anions to reduce the surface area. Notably, the counter anions occupy some spaces within the networks of these porous polymers, more or less leading to reduced surface areas.[81] On the other hand, for the ionic porous polymers with *C*3-symmetry, the rigidity of skeletons was more or less weakened by the tritopic building blocks comprising phenyl and/or triazine rings, which could create much more complex conformational torsions by free rotation around single carbon–carbon bonds, and also tends to cause the interpenetration of chain segments. Correspondingly, these three porous polymers show lower specific surface areas.[82,83]

Table 2 Surface area, pore volume, and pore size for synthesized *C*3-symmetry ionic polymers

	Surface area (m^2 g^{-1})			Pore volume (cm^3 g^{-1})		Pore size (nm)	
Sample code	BET	BJH	DFT	BJH	DFT	BJH	DFT
PPyTri-O$_{\mathrm{Cl}}$	54.73	58.40	52.83	0.17	0.17	5.7	6.9
PPyTri-O$_{\mathrm{PF6}}$	60.57	64.66	57.73	0.18	0.18	5.7	6.3
PPyTri-O$_{\mathrm{TFSI}}$	35.00	26.76	33.78	0.11	0.10	5.7	6.3
PPyBz-O$_{\mathrm{Br}}$	50.76	34.18	54.49	0.19	0.19	5.7	6.3
PPyBz-O$_{\mathrm{PF6}}$	53.84	56.30	56.61	0.21	0.19	5.7	6.3
PPyBz-O$_{\mathrm{TFSI}}$	46.15	37.60	46.35	0.15	0.15	5.7	6.3

3.5. QCN study

3.5.1 Sensor activity of PPyTri-O and PPyBz-O derivatives on QCN chips for CO$_2$ gas sensing. The detection of CO$_2$ on the surface of porous ionic polymers (PIPs) sensors was performed and measured using QCN. A comparative frequency shift (Δ*f*) analysis of CO$_2$ gas exposure across **PPyTri-O** and **PPyBz-O** derivatives films at 20 °C, 25 °C, and 30 °C was performed. The process was conducted sequentially at each temperature, providing sufficient time for the QCN chips to stabilize after each temperature adjustment, and the baseline frequency (*f*0) for each PIP sensor was recorded before CO$_2$ gas exposure.[84–86] Fig. 5 illustrates the monitoring of the frequency shift (Δ*f*) for each individual PIPs sensor while the CO$_2$ gas is introduced into the chamber. The (Δ*f*) values and the average of (Δ*f*) were recorded for every CO$_2$ concentration level ranging from low to hundreds of ppm. Upon the introduction of CO$_2$ gas to the sensors, it was observed that the frequency decreased rapidly, and the response time of the **PPyTri-O** and **PPyBz-O** derivatives was established as the time required for the frequency shift to reduce by ∼85% upon activation of the gas. The polymers **PPyTri-O$_{\mathrm{PF6}}$** and **PPyBz-O$_{\mathrm{PF6}}$** displayed the highest adsorption of CO$_2$ on their surfaces, followed by **PPyTri-O$_{\mathrm{Cl}}$** and **PPyBz-O$_{\mathrm{Br}}$**, while the **PPyBz-O$_{\mathrm{TFSI}}$** and **PPyTri-O$_{\mathrm{TFSI}}$** recorded the least

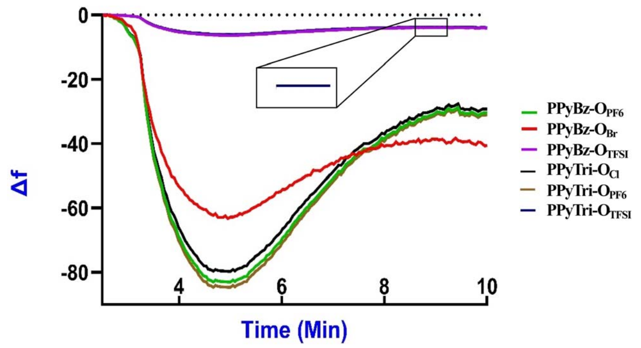

Fig. 5 QCN sensorgram curves of PPyTri-O and PPyBz-O thin film derivatives showing the response to CO$_2$ gas at 25 °C.

response. The response time for the four polymers was between 4 to 5 min. As the gas molecules were adsorbed onto the surface of the sensitive film, the sensors reached a steady state. When the CO_2 gas was purged from the sensors using clean N_2, the frequency returned to its original level, and the sensors demonstrated quick recovery with approximately 2 min. These data demonstrated that the type of counter anion significantly influences the CO_2 adsorption capacity of PIPs. Among the four polymers, the ionic polymers with PF_6 as the counter anion attained the best results, followed closely by PIPs containing halogens and those with TFSI were the last. These results were consistent with the surface area findings derived from the BET model theory, where the PIPs displayed a surface area in the same order as their response to CO_2 adsorption, PF_6 >Cl, Br > TFSI. The obtained results are in agreement with those from the prior research on polymerization-derived PIPs,[81,82] which indicated that inorganic anions such as halogens and PF_6 provided the most effective CO_2 adsorption. This concludes that selecting the right anion is crucial for achieving high CO_2 detection performance and increasing the CO_2 adsorption on the surface of the formed sensor. Furthermore, the influence of the cations on the CO_2 detection comes right after the anions impact and can be observed in the difference responses between PIPs with triazine and benzene cores in **PPyTri-O$_{PF6}$** and **PPyBz-O$_{PF6}$** as well as in **PPyTri-O$_{Cl}$** and **PPyBz-O$_{Br}$**. The ionic polymers with triazine entities showed a higher affinity for CO_2 than those with a benzene core, which can be predicted by the effect of C–N linkages on attractive CO_2 adsorption.[87]

3.5.2 Precision analysis.

The precision of the PIP sensors was assessed by calculating the standard deviations of the Δ*f* values after 25 minutes of gas exposure for the PIP sensors on the QCN chips (Fig. 6). The analysis confirmed that the mean frequency shifts of the sensors were consistent with 25 minutes CO_2 gas exposure experiments at different temperatures (Fig. 7).

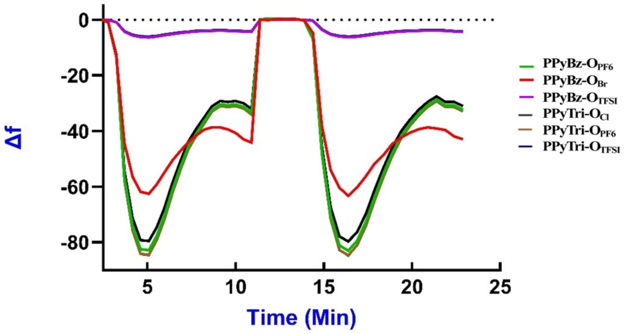

Fig. 7 Sensorgram curves of PIPs after 25 minutes of exposure showing a high level of precision of the sensors.

Fig. 6 and 7 depict the mean Δ*f* values for the sensors, and the standard deviation of the repeated exposures ranged from 8.98 to 9.65 Hz, indicating a high level of precision and repeatability. These results demonstrate the exceptional precision and reliability of the PIP sensors for CO_2 gas detection at temperatures between 20 °C and 30 °C. According to the data in Fig. 6, it can be observed that the impact of the temperature on the frequency shift becomes more pronounced as the temperature rises from 20 °C to 30 °C.

3.5.3 Selectivity, reproducibility, and sensitivity.

The selectivity of the fabricated PIP sensors on QCN chips for CO_2 gas sensing at varying temperatures was studied in comparison to non-targeted gases such as NH_3 and H_2S (Fig. 6 and S5†). The obtained sensors outperformed the selectivity toward CO_2 gas in comparison with NH_3 and H_2S as the Δ*f* values decreased, indicating CO_2 gas adsorption on the surface. In contrast, the decrease in Δ*f* values for NH_3 and H_2S indicates the non-sensing of these gases (Fig. S5†). These findings demonstrate the exceptional CO_2 selectivity of the sensors at different

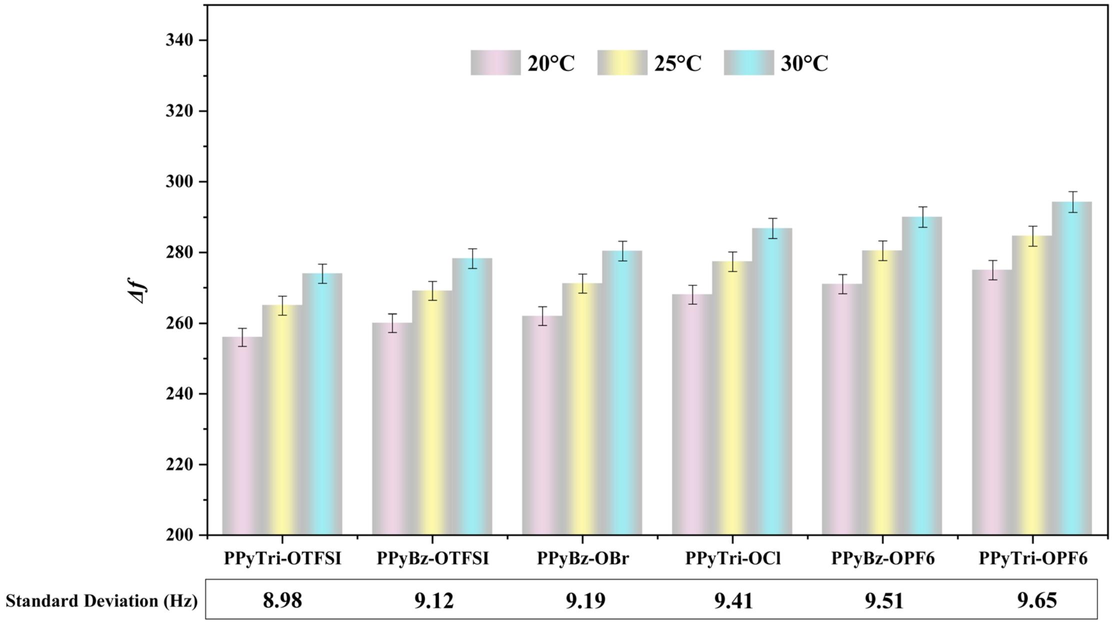

	PPyTri-OTFSI	PPyBz-OTFSI	PPyBz-OBr	PPyTri-OCl	PPyBz-OPF6	PPyTri-OPF6
Standard Deviation (Hz)	8.98	9.12	9.19	9.41	9.51	9.65

Fig. 6 The average frequency shift (Δ*f*) and standard deviation for each PIP sensor at 20 °C, 25 °C, and 30 °C.

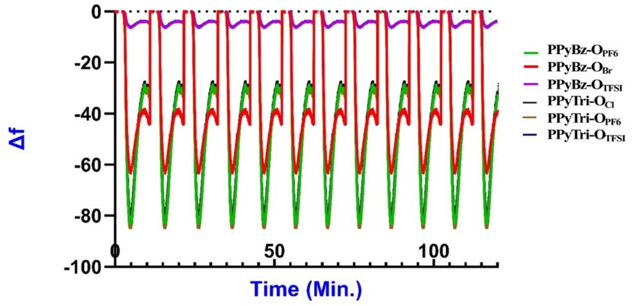

Fig. 8 The repeatability response sensorgram curves of PIPs for multiple cycles.

temperatures, making them a suitable choice for CO_2 detection applications.

The reproducibility test was undertaken through multiple repeated measurements of the frequency shift (Δf) for randomly chosen PIPs at three temperatures (20 °C, 25 °C, and 30 °C). The relative standard deviations (RSD) of the Δf values were computed to evaluate the sensors' reproducibility. Table S1† and Fig. (8) exhibit the frequency shift measurements (Δf) and RSD (%) values for the samples, respectively. The RSD values in the table indicate that the frequency shifts between the triplicate measurements demonstrate a high level of reproducibility, and the outcomes in the figures for each run were stable and indistinguishable, as there were no noticeable differences in the response. These results demonstrate the dependability of the designed sensors when exposed to CO_2 gas under various temperature conditions.

Evaluating the efficiency of the formed sensors on the QCN chips as CO_2 gas sensors at various temperatures provides vital information regarding the capabilities of the sensors. Sensitivity can be represented as the change in the frequency (Δf) per unit concentration of CO_2 and can be calculated by dividing the average frequency shift (Δf) by CO_2 concentration.

3.5.4 Mechanism of action. The fabricated PIP sensors on quartz crystal nanobalance (QCN) chips detected CO_2 gas by leveraging the CO_2 affinity of Lewis acidic groups within the PIPs. When CO_2 molecules permeate the sensor phase, the polymer chains undergo structural changes, increasing rigidity. This rigidification due to CO_2 adsorption causes a steady frequency shift. The primary transduction mechanism involves depositing polymer film layers containing CO_2-philic moieties (*e.g.*, PF_6) onto the piezoelectric quartz crystal surface. When CO_2 gas interacts with the PIP sensor, the polar moieties of the porous ionic polymer form host–guest complexes with CO_2 molecules, increasing the overall mass and reducing conformational chain flexibility, which stiffens the PIP film. Consequently, the frequency shift (Δf) is directly proportional to mass change (Δm) and inversely proportional to the square of the base resonance frequency ($f0$), as described by the Sauerbrey equation:

$$\Delta f = -(2 \cdot f0^2 \cdot \Delta m)/(A \cdot \rho \cdot \sqrt{\mu})$$

where A is the electrode area, ρ is the density of quartz, and μ is the shear modulus.

The designed PIP sensors on QCN chips enable precise, selective, and reproducible CO_2 measurements due to the stability of the physisorption process. This process forms weak intermolecular bonds between the CO_2 molecules and the PIP-coated QCN chip surface, ensuring stable and continuous linkages during gas adsorption and desorption.

To contextualize the performance of the synthesized porous ionic polymers for CO_2 sensing, a comparison was made with the previously reported QCM-based sensing materials. Table 3 summarizes the frequency shifts observed for CO_2 detection using various materials, alongside their selectivity toward interfering gases such as NH_3 and H_2S. Ethyl cellulose (EC) exhibited strong CO_2 responsiveness, while polypyrrole (PPy) demonstrated limited sensitivity. Tetramethylammonium fluoride tetrahydrate (TMAF) and polyethyleneimine (PEI) showed substantial CO_2 responses; however, their cross-sensitivity to NH_3 and SO_2 limits their practical applicability. Similarly, nitrogen-doped tungsten carbide (WC@NC) provided excellent

Table 3 Sensing of CO_2 and selectivity over H_2S and NH_3 in PIPs and some reported materials

Material	Frequency shift for CO_2 (Hz)	Selectivity CO_2 over H_2S	Selectivity CO_2 over NH_3	Notes	Ref.
Ethyl cellulose (EC)	438.95	Moderate	Low	Strong CO_2 response; limited cross-responsiveness	88
Polypyrrole (PPy)	59.00	Low	Low	Modest sensitivity to CO_2, mainly used in gas mixture detection	
Tetramethylammonium fluoride (TMAF)	300.80	Moderate	Low	Good CO_2 sensitivity but notable responses to SO_2 and NH_3	
Polyethyleneimine (PEI)	980.78	Low	Low	Exceptional response to NH_3, making it less selective for CO_2	
WC@NC (nitrogen-doped tungsten carbide)	11.78	Low	Low	Excellent H_2S selectivity but minimal CO_2 sensitivity	
PPyTri-O$_{TFSI}$	264.96	High	High	High CO_2 sensitivity with excellent selectivity over H_2S and NH_3; thermally stable	This work
PPyBz-O$_{TFSI}$	269.10	High	High		
PPyBz-O$_{Br}$	271.17	High	High		
PPyTri-O$_{Cl}$	277.38	High	High		
PPyBz-O$_{PF6}$	280.49	High	High		
PPyTri-O$_{PF6}$	284.63	High	High		

selectivity for H_2S but showed minimal sensitivity to CO_2. In comparison, the newly developed porous ionic polymers (*e.g.*, **PPyTri-O$_{\mathbf{TFSI}}$**, **PPyBz-O$_{\mathbf{TFSI}}$**, and **PPyTri-O$_{\mathbf{PF6}}$**) exhibited high CO_2 sensitivity with frequency shifts ranging from 264.96 Hz to 284.63 Hz, demonstrating superior performance compared to the previously reported materials. Furthermore, these polymers exhibited exceptional selectivity for CO_2, with minimal interference from NH_3 and H_2S, which is critical for real-world applications. The tunable performance of these polymers, achieved through structural modifications and tailored anion incorporation, further underscores their potential as next-generation materials for precise and selective CO_2 sensing.

4. Conclusions

An efficient quaternization of the designed 4,4′-dipyridyl derivative **4,4′-bp-O** with the appropriate 1,3,5-tris(-bromomethyl)benzene **BB** and/or cyanuric chloride **CC** resulted in the effective synthesis of a new class of porous ionic polymers tethering triazine (benzene) nucleus conjugated to three pyridiniums as cationic counterparts tethered bromide/chloride anions **PPyBz-O** and **PPyTri-O**. LiTFSI and KPF_6 anions were incorporated into the core of such polymers through a metathesis protocol furnished on the formation of new ionic polymers. The structures of the formed polymers were investigated by FTIR, ^{1}H NMR, and ^{13}C NMR analyses. The synthesized polymer was analyzed using PXRD, which showed the presence of semi-crystalline structures. The SEM examination demonstrated that micro or nanoparticles were uniformly distributed within the polymer. Furthermore, the TGA and DTA analyses indicated that the synthesized polymers exhibited good thermal stability. The modified porous ionic polymer was tested for CO_2 gas sensing using quartz crystal nanobalance (QCN), which demonstrated precise, selective, and reproducible measurements.

Data availability

The authors confirm that all data are included in the manuscript.

Conflicts of interest

There are no conflicts to declare.

Acknowledgements

This project was funded by the Deanship of Scientific Research (DSR) at King Abdulaziz University, Jeddah, under grant no. (GPIP: 1193-130-2024). The authors, therefore, acknowledge with thanks DSR for technical and financial support.

References

1 S.-J. Chen, D. C. Hovde, K. A. Peterson and A. W. Marshall, “Fire detection using smoke and gas sensors”, *Fire Saf. J.*, 2007, **42**(8), 507–515, DOI: 10.1016/j.firesaf.2007.01.006.

2 A. De Pinto, *et al.*, “Low Emission Development Strategies in Agriculture. An Agriculture, Forestry, and Other Land Uses (AFOLU) Perspective”, *World Dev.*, 2016, **87**, 180–203, DOI: 10.1016/j.worlddev.2016.06.013.

3 C. Jiang, M. K. Masood, Y. C. Soh and H. Li, “Indoor occupancy estimation from carbon dioxide concentration”, *Energy Build.*, 2016, **131**, 132–141, DOI: 10.1016/j.enbuild.2016.09.002.

4 Z. A. Siefker, *et al.*, “Manipulating polymer composition to create low-cost, high-fidelity sensors for indoor CO_2 monitoring”, *Sci. Rep.*, 2021, **11**(1), 13237, DOI: 10.1038/s41598-021-92181-4.

5 M. Chatterjee, *et al.*, “A rate-based transcutaneous CO_2 sensor for noninvasive respiration monitoring”, *Physiol. Meas.*, 2015, **36**(5), 883–894, DOI: 10.1088/0967-3334/36/5/883.

6 C. G. Cooney, B. C. Towe and C. R. Eyster, “Optical pH, oxygen and carbon dioxide monitoring using a microdialysis approach”, *Sens. Actuators, B*, 2000, **69**(1–2), 183–188, DOI: 10.1016/S0925-4005(00)00544-X.

7 A. Mills, A. Lepre and L. Wild, “Breath-by-breath measurement of carbon dioxide using a plastic film optical sensor”, *Sens. Actuators, B*, 1997, **39**(1–3), 419–425, DOI: 10.1016/S0925-4005(96)02116-8.

8 G. Neurauter, I. Klimant and O. S. Wolfbeis, “Fiber-optic microsensor for high resolution pCO_2 sensing in marine environment”, *Fresenius. J. Anal. Chem.*, 2000, **366**(5), 481–487, DOI: 10.1007/s002160050097.

9 S. Neethirajan, D. S. Jayas and S. Sadistap, “Carbon Dioxide (CO_2) Sensors for the Agri-food Industry—A Review”, *Food Bioprocess Technol.*, 2009, **2**(2), 115–121, DOI: 10.1007/s11947-008-0154-y.

10 P. Puligundla, J. Jung and S. Ko, “Carbon dioxide sensors for intelligent food packaging applications”, *Food Control*, 2012, **25**(1), 328–333, DOI: 10.1016/j.foodcont.2011.10.043.

11 A. Bulbul and H. Kim, “A bubble-based microfluidic gas sensor for gas chromatographs”, *Lab Chip*, 2015, **15**(1), 94–104, DOI: 10.1039/C4LC00892H.

12 T.-V. Dinh, I.-Y. Choi, Y.-S. Son and J.-C. Kim, “A review on non-dispersive infrared gas sensors: Improvement of sensor detection limit and interference correction”, *Sens. Actuators, B*, 2016, **231**, 529–538, DOI: 10.1016/j.snb.2016.03.040.

13 L. Yu, *et al.*, “A fluorescence probe for highly selective and sensitive detection of gaseous ozone based on excited-state intramolecular proton transfer mechanism”, *Sens. Actuators, B*, 2018, **266**, 717–723, DOI: 10.1016/j.snb.2018.03.175.

14 Y. Yan, *et al.*, “Sensitive detection of sulfide based on the self-assembly of fluorescent silver nanoclusters on the surface of silica nanospheres”, *Talanta*, 2017, **174**, 387–393, DOI: 10.1016/j.talanta.2017.06.027.

15 M. Sun, *et al.*, “Palladacycle Based Fluorescence Turn-On Probe for Sensitive Detection of Carbon Monoxide”, *ACS Sens.*, 2018, **3**(2), 285–289, DOI: 10.1021/acssensors.7b00835.

16 T. Yang, W. Chen and P. Wang, “A review of all-optical photoacoustic spectroscopy as a gas sensing method”,

Appl. Spectrosc. Rev., 2021, **56**(2), 143–170, DOI: 10.1080/05704928.2020.1760875.

17 S. Neethirajan, M. S. Freund, D. S. Jayas, C. Shafai, D. J. Thomson and N. D. G. White, "Development of carbon dioxide (CO_2) sensor for grain quality monitoring", *Biosyst. Eng.*, 2010, **106**(4), 395–404, DOI: 10.1016/j.biosystemseng.2010.05.002.

18 N. B. Borchert, J. P. Kerry and D. B. Papkovsky, "A CO_2 sensor based on Pt-porphyrin dye and FRET scheme for food packaging applications", *Sens. Actuators, B*, 2013, **176**, 157–165, DOI: 10.1016/j.snb.2012.09.043.

19 A. Mirmohseni, K. Farhadi and S. Jahangiri, "Application of polydimethylsiloxane/acrylic resins coated quartz crystal nano balance sensor for detection of glyphosate pesticide", *Int. J. Environ. Anal. Chem.*, 2020, **100**(7), 733–745, DOI: 10.1080/03067319.2019.1639687.

20 G. Barandun, *et al.*, "Cellulose Fibers Enable Near-Zero-Cost Electrical Sensing of Water-Soluble Gases", *ACS Sens.*, 2019, **4**(6), 1662–1669, DOI: 10.1021/acssensors.9b00555.

21 R. Alrammouz, J. Podlecki, P. Abboud, B. Sorli and R. Habchi, "A review on flexible gas sensors: From materials to devices", *Sens. Actuators, A*, 2018, **284**, 209–231, DOI: 10.1016/j.sna.2018.10.036.

22 S. Demirci, "Crosslinked-Polymer Brushes with Switchable Capture and Release Capabilities", *Polymers*, 2018, **10**(9), 956, DOI: 10.3390/polym10090956.

23 A. Darabi, J. Glasing, P. G. Jessop and M. F. Cunningham, "Preparation of CO_2-switchable latexes using *N*-[3-(dimethylamino)propyl]-methacrylamide (DMAPMAm)", *J. Polym. Sci., Part A:Polym. Chem.*, 2017, **55**(6), 1059–1066, DOI: 10.1002/pola.28466.

24 T. C. D. Doan, J. Baggerman, R. Ramaneti, H. D. Tong, A. T. M. Marcelis and C. J. M. Van Rijn, "Carbon dioxide detection with polyethylenimine blended with polyelectrolytes", *Sens. Actuators, B*, 2014, **201**, 452–459, DOI: 10.1016/j.snb.2014.05.023.

25 M. F. Cunningham and P. G. Jessop, "An introduction to the principles and fundamentals of CO_2-switchable polymers and polymer colloids", *Eur. Polym. J.*, 2016, **76**, 208–215, DOI: 10.1016/j.eurpolymj.2016.01.036.

26 Z. Guo, Y. Feng, Y. Wang, J. Wang, Y. Wu and Y. Zhang, "A novel smart polymer responsive to CO_2", *Chem. Commun.*, 2011, **47**(33), 9348, DOI: 10.1039/c1cc12388b.

27 Q. Yan, R. Zhou, C. Fu, H. Zhang, Y. Yin and J. Yuan, "CO_2-Responsive Polymeric Vesicles that Breathe", *Angew. Chem., Int. Ed.*, 2011, **50**(21), 4923–4927, DOI: 10.1002/anie.201100708.

28 J. Y. Quek, P. J. Roth, R. A. Evans, T. P. Davis and A. B. Lowe, "Reversible addition–fragmentation chain transfer synthesis of amidine-based, CO_2-responsive homo and AB diblock (Co)polymers comprised of histamine and their gas-triggered self-assembly in water", *J. Polym. Sci., Part A:Polym. Chem.*, 2013, **51**(2), 394–404, DOI: 10.1002/pola.26397.

29 H. Liu, Y. Zhao, C. A. Dreiss and Y. Feng, "CO_2-switchable multi-compartment micelles with segregated corona", *Soft Matter*, 2014, **10**(34), 6387–6391, DOI: 10.1039/C4SM01207K.

30 Q. Yan and Y. Zhao, "CO_2-Stimulated Diversiform Deformations of Polymer Assemblies", *J. Am. Chem. Soc.*, 2013, **135**(44), 16300–16303, DOI: 10.1021/ja408655n.

31 H. Liu, S. Lin, Y. Feng and P. Theato, "CO_2-Responsive polymer materials", *Polym. Chem.*, 2017, **8**(1), 12–23, DOI: 10.1039/C6PY01101B.

32 A. K. Alshamrani, J. R. Vanderveen and P. G. Jessop, "A guide to the selection of switchable functional groups for CO_2-switchable compounds", *Phys. Chem. Chem. Phys.*, 2016, **18**(28), 19276–19288, DOI: 10.1039/C6CP03302D.

33 M. F. Cunningham and P. G. Jessop, "Carbon Dioxide-Switchable Polymers: Where Are the Future Opportunities?", *Macromolecules*, 2019, **52**(18), 6801–6816, DOI: 10.1021/acs.macromol.9b00914.

34 Y. Shi, J. Yang, F. Gao and Q. Zhang, "Covalent Organic Frameworks: Recent Progress in Biomedical Applications", *ACS Nano*, 2023, **17**(3), 1879–1905, DOI: 10.1021/acsnano.2c11346.

35 Y. Zhu, P. Xu, X. Zhang and D. Wu, "Emerging porous organic polymers for biomedical applications", *Chem. Soc. Rev.*, 2022, **51**(4), 1377–1414, DOI: 10.1039/D1CS00871D.

36 M. Al Sharabati, R. Sabouni and G. A. Husseini, "Biomedical Applications of Metal–Organic Frameworks for Disease Diagnosis and Drug Delivery: A Review", *Nanomaterials*, 2022, **12**(2), 277, DOI: 10.3390/nano12020277.

37 L. Yue, K. Yang, X.-Y. Lou, Y.-W. Yang and R. Wang, "Versatile Roles of Macrocycles in Organic–Inorganic Hybrid Materials for Biomedical Applications", *Matter*, 2020, **3**(5), 1557–1588, DOI: 10.1016/j.matt.2020.09.019.

38 H. Ma, *et al.*, "Microstructure Manipulation of Covalent Organic Frameworks (COFs)-based Membrane for Efficient Separations", *Chem. Res. Chin. Univ.*, 2022, **38**(2), 325–338, DOI: 10.1007/s40242-022-1474-6.

39 Z. Wang, S. Zhang, Y. Chen, Z. Zhang and S. Ma, "Covalent organic frameworks for separation applications", *Chem. Soc. Rev.*, 2020, **49**(3), 708–735, DOI: 10.1039/C9CS00827F.

40 K. Geng, *et al.*, "Covalent Organic Frameworks: Design, Synthesis, and Functions", *Chem. Rev.*, 2020, **120**(16), 8814–8933, DOI: 10.1021/acs.chemrev.9b00550.

41 F. J. Uribe-Romo, J. R. Hunt, H. Furukawa, C. Klöck, M. O'Keeffe and O. M. Yaghi, "A Crystalline Imine-Linked 3-D Porous Covalent Organic Framework", *J. Am. Chem. Soc.*, 2009, **131**(13), 4570–4571, DOI: 10.1021/ja8096256.

42 V. Stavila, A. A. Talin and M. D. Allendorf, "MOF-based electronic and opto-electronic devices", *Chem. Soc. Rev.*, 2014, **43**(16), 5994–6010, DOI: 10.1039/C4CS00096J.

43 F. Yu, W. Liu, S.-W. Ke, M. Kurmoo, J.-L. Zuo and Q. Zhang, "Electrochromic two-dimensional covalent organic framework with a reversible dark-to-transparent switch", *Nat. Commun.*, 2020, **11**(1), 5534, DOI: 10.1038/s41467-020-19315-6.

44 S. Xu and Q. Zhang, "Recent progress in covalent organic frameworks as light-emitting materials", *Mater. Today Energy*, 2021, **20**, 100635, DOI: 10.1016/j.mtener.2020.100635.

45 F. Yu, W. Liu, B. Li, D. Tian, J. Zuo and Q. Zhang, "Photostimulus-Responsive Large-Area Two-Dimensional

Covalent Organic Framework Films", *Angew. Chem., Int. Ed.*, 2019, **58**(45), 16101–16104, DOI: **10.1002/anie.201909613**.

46 V. Singh, *et al.*, "Thiazole-Linked Covalent Organic Framework Promoting Fast Two-Electron Transfer for Lithium-Organic Batteries", *Adv. Energy Mater.*, 2021, **11**(17), 2003735, DOI: **10.1002/aenm.202003735**.

47 X. Yang, *et al.*, "Mesoporous Polyimide-Linked Covalent Organic Framework with Multiple Redox-Active Sites for High-Performance Cathodic Li Storage", *Angew. Chem., Int. Ed.*, 2022, **61**(31), e202207043, DOI: **10.1002/anie.202207043**.

48 X. Luo, *et al.*, "Covalent Organic Framework with Highly Accessible Carbonyls and π-Cation Effect for Advanced Potassium-Ion Batteries", *Angew. Chem., Int. Ed.*, 2022, **61**(10), e202117661, DOI: **10.1002/anie.202117661**.

49 S. Zheng, *et al.*, "Orthoquinone–Based Covalent Organic Frameworks with Ordered Channel Structures for Ultrahigh Performance Aqueous Zinc–Organic Batteries", *Angew. Chem.*, 2022, **134**(12), e202117511, DOI: **10.1002/ange.202117511**.

50 L. Zhong, Z. Fang, C. Shu, C. Mo, X. Chen and D. Yu, "Redox Donor–Acceptor Conjugated Microporous Polymers as Ultralong-Lived Organic Anodes for Rechargeable Air Batteries", *Angew. Chem., Int. Ed.*, 2021, **60**(18), 10164–10171, DOI: **10.1002/anie.202016746**.

51 F. R. Fortea-Pérez, *et al.*, "The MOF-driven synthesis of supported palladium clusters with catalytic activity for carbene-mediated chemistry", *Nat. Mater.*, 2017, **16**(7), 760–766, DOI: **10.1038/nmat4910**.

52 Q. Sun, Z. Dai, X. Meng and F.-S. Xiao, "Porous polymer catalysts with hierarchical structures", *Chem. Soc. Rev.*, 2015, **44**(17), 6018–6034, DOI: **10.1039/C5CS00198F**.

53 X. Wang, X. Han, J. Zhang, X. Wu, Y. Liu and Y. Cui, "Homochiral 2D Porous Covalent Organic Frameworks for Heterogeneous Asymmetric Catalysis", *J. Am. Chem. Soc.*, 2016, **138**(38), 12332–12335, DOI: **10.1021/jacs.6b07714**.

54 W. Tu, Y. Xu, S. Yin and R. Xu, "Rational Design of Catalytic Centers in Crystalline Frameworks", *Adv. Mater.*, 2018, **30**(33), 1707582, DOI: **10.1002/adma.201707582**.

55 R. K. Sharma, *et al.*, "Recent development of covalent organic frameworks (COFs): synthesis and catalytic (organic-electro-photo) applications", *Mater. Horiz.*, 2020, **7**(2), 411–454, DOI: **10.1039/C9MH00856J**.

56 K. Xu and N. Huang, "Recent Advances of Covalent Organic Frameworks in Chemical Sensing", *Chem. Res. Chin. Univ.*, 2022, **38**(2), 339–349, DOI: **10.1007/s40242-022-1476-4**.

57 Y. Li, L. Li and J. Yu, "Applications of Zeolites in Sustainable Chemistry", *Chem*, 2017, **3**(6), 928–949, DOI: **10.1016/j.chempr.2017.10.009**.

58 C. A. Trickett, A. Helal, B. A. Al-Maythalony, Z. H. Yamani, K. E. Cordova and O. M. Yaghi, "The chemistry of metal–organic frameworks for CO_2 capture, regeneration and conversion", *Nat. Rev. Mater.*, 2017, **2**(8), 17045, DOI: **10.1038/natrevmats.2017.45**.

59 S. Zeng, *et al.*, "Ionic-Liquid-Based CO_2 Capture Systems: Structure, Interaction and Process", *Chem. Rev.*, 2017, **117**(14), 9625–9673, DOI: **10.1021/acs.chemrev.7b00072**.

60 Q. Sun, Y. Jin, B. Aguila, X. Meng, S. Ma and F. Xiao, "Porous Ionic Polymers as a Robust and Efficient Platform for Capture and Chemical Fixation of Atmospheric CO_2", *ChemSusChem*, 2017, **10**(6), 1160–1165, DOI: **10.1002/cssc.201601350**.

61 A. E. Creamer and B. Gao, "Carbon-Based Adsorbents for Postcombustion CO_2 Capture: A Critical Review", *Environ. Sci. Technol.*, 2016, **50**(14), 7276–7289, DOI: **10.1021/acs.est.6b00627**.

62 L. Tao, F. Niu, J. Liu, T. Wang and Q. Wang, "Troger's base functionalized covalent triazine frameworks for CO_2 capture", *RSC Adv.*, 2016, **6**(97), 94365–94372, DOI: **10.1039/C6RA21196H**.

63 L. Zou, *et al.*, "Porous Organic Polymers for Post-Combustion Carbon Capture", *Adv. Mater.*, 2017, **29**(37), 1700229, DOI: **10.1002/adma.201700229**.

64 M. Carta, M. Croad, K. Bugler, K. J. Msayib and N. B. McKeown, "Heterogeneous organocatalysts composed of microporous polymer networks assembled by Tröger's base formation", *Polym. Chem.*, 2014, **5**(18), 5262, DOI: **10.1039/C4PY00608A**.

65 S. Das, P. Heasman, T. Ben and S. Qiu, "Porous Organic Materials: Strategic Design and Structure–Function Correlation", *Chem. Rev.*, 2017, **117**(3), 1515–1563, DOI: **10.1021/acs.chemrev.6b00439**.

66 N. Chaoui, M. Trunk, R. Dawson, J. Schmidt and A. Thomas, "Trends and challenges for microporous polymers", *Chem. Soc. Rev.*, 2017, **46**(11), 3302–3321, DOI: **10.1039/C7CS00071E**.

67 S. Muraoka, Y. Kiyohara, H. Oue and S. Higashimoto, "A CO_2 Sensor Using a Quartz Crystal Microbalance Coated with a Sensitive Membrane", *Electron. Commun. Jpn.*, 2014, **97**(2), 60–66, DOI: **10.1002/ecj.11601**.

68 M. T. S. R. Gomes, P. S. T. Nogueira and J. A. B. P. Oliveira, "Quantification of CO_2, SO_2, NH_3, and H_2S with a single coated piezoelectric quartz crystal", *Sens. Actuators, B*, 2000, **68**(1–3), 218–222, DOI: **10.1016/S0925-4005(00)00432-9**.

69 X. Liu, G. He, X. Huang, Y. Zhuang and J. Hou, "Detection of CO_2, H_2S, NH_3, and gas mixtures using a quartz crystal microbalance sensor array with five sensitive materials", *Measurement*, 2025, **242**, 115891, DOI: **10.1016/j.measurement.2024.115891**.

70 K. Cai, *et al.*, "Construction of bifunctional triazine-based imidazolium porous ionomer polymers by a post-crosslinking tactic for efficient CO_2 capture and conversion", *Chem. Eng. J.*, 2023, **451**, 138946, DOI: **10.1016/j.cej.2022.138946**.

71 Y. Li, *et al.*, "A composite solid polymer electrolyte incorporating MnO2 nanosheets with reinforced mechanical properties and electrochemical stability for lithium metal batteries", *J. Mater. Chem. A*, 2020, **8**(4), 2021–2032, DOI: **10.1039/C9TA11542K**.

72 A. A. Raja and C. T. Yavuz, "Charge induced formation of crystalline network polymers", *RSC Adv.*, 2014, **4**(104), 59779–59784, DOI: **10.1039/C4RA10594J**.

73 Y. Biswas, P. Banerjee and T. K. Mandal, "From Polymerizable Ionic Liquids to Poly(ionic liquid)s: Structure-Dependent Thermal, Crystalline, Conductivity, and Solution Thermoresponsive Behaviors", *Macromolecules*, 2019, **52**(3), 945–958, DOI: **10.1021/acs.macromol.8b02351**.

74 E. M. Maya, E. Verde-Sesto, D. Mantione, M. Iglesias and D. Mecerreyes, "New poly(ionic liquid)s based on poly(azomethine-pyridinium) salts and its use as heterogeneous catalysts for CO_2 conversion", *Eur. Polym. J.*, 2019, **110**, 107–113, DOI: **10.1016/j.eurpolymj.2018.07.030**.

75 W. Lin, *et al.*, "Novel triazine-based cationic covalent organic polymers for highly efficient and selective removal of selenate from contaminated water", *J. Hazard. Mater.*, 2022, **436**, 129127, DOI: **10.1016/j.jhazmat.2022.129127**.

76 S. Hou, M. Meng, D. Liu and P. Zhang, "Mechanochemical Process to Construct Porous Ionic Polymers by Menshutkin Reaction", *ChemSusChem*, 2021, **14**(15), 3059–3063, DOI: **10.1002/cssc.202101093**.

77 W. Li, *et al.*, "Design of Thiazolo[5,4-*d*]thiazole-Bridged Ionic Covalent Organic Polymer for Highly Selective Oxygen Reduction to H $_2$ O $_2$", *Chem. Mater.*, 2020, **32**(19), 8553–8560, DOI: **10.1021/acs.chemmater.0c02843**.

78 K. S. W. Sing, *"Reporting physisorption data for gas/solid systems with special reference to the determination of surface area and porosity"*, 1984, DOI: **10.1351/pac198557040603**.

79 M. Wang, Z. Li, Z. Liang, Z. Jiang and W. Wu, "Method Selection for Analyzing the Mesopore Structure of Shale—Using a Combination of Multifractal Theory and Low-Pressure Gas Adsorption", *Energies*, 2023, **16**(5), 2464, DOI: **10.3390/en16052464**.

80 S. E. Fazli, M. Mirzaei, S. Mohammadinejad, and H. Fazli, *"Impact of flexibility on the aggregation of polymeric macromolecules | The European Physical Journal E"*, doi: DOI: **10.1140/epje/s10189-023-00324-4**.

81 K. Cai, *et al.*, "Imidazolium- and triazine-based ionic polymers as recyclable catalysts for efficient fixation of CO_2 into cyclic carbonates", *J. CO_2 Util.*, 2021, **51**, 101658, DOI: **10.1016/j.jcou.2021.101658**.

82 J. Lin, *et al.*, "A metal-free approach to bipyridinium salt-based conjugated porous polymers with olefin linkages", *Polym. Chem.*, 2021, **12**(11), 1661–1667, DOI: **10.1039/D0PY01743D**.

83 A. Liu, J. Zhang and X. Lv, "Novel hydrazine-bridged covalent triazine polymer for CO_2 capture and catalytic conversion", *Chin. J. Catal.*, 2018, **39**(8), 1320–1328, DOI: **10.1016/S1872-2067(18)63040-2**.

84 R. Li, Y. Fan, Z. Ma, D. Zhang, Y. Liu and J. Xu, "Controllable preparation of ultrathin MXene nanosheets and their excellent QCM humidity sensing properties enhanced by fluoride doping", *Microchim. Acta*, 2021, **188**(3), 81, DOI: **10.1007/s00604-021-04723-2**.

85 B. Sun, G. Xie, Y. Jiang and X. Li, "Comparative CO_2-Sensing Characteristic Studies of PEI and PEI/Starch Thin Film Sensors", *Energy Procedia*, 2011, **12**, 726–732, DOI: **10.1016/j.egypro.2011.10.098**.

86 M. Berouaken *et al.*, "CO_2 Gas Sensors Based on Hydrophilic Vanadium Oxide Thin Film Coated QCM", in *Springer Proceedings in Energy*, ICREEC 2019, ed. A. Belasri and S. A. Beldjilali, Springer, Singapore, 2020, pp. 633–638, DOI: **10.1007/978-981-15-5444-5_79**.

87 S. Gu, *et al.*, "1,3,5-Triazine-Based Microporous Polymers with Tunable Porosities for CO_2 Capture and Fluorescent Sensing", *Macromolecules*, 2017, **50**(21), 8512–8520, DOI: **10.1021/acs.macromol.7b01857**.

88 X. Liu, G. He, X. Huang, Y. Zhuang and J. Hou, "Detection of CO_2, H_2S, NH_3, and gas mixtures using a quartz crystal microbalance sensor array with five sensitive materials", *Measurement*, 2025, **242**, 115891, DOI: **10.1016/j.measurement.2024.115891**.